energies

MDPI

Article

In-Stream Energy by Tidal and Wind-Driven Currents: An Analysis for the Gulf of California

Vanesa Magar [1,*,†], Victor M. Godínez [1,†], Markus S. Gross [1], Manuel López-Mariscal [1], Anahí Bermúdez-Romero [1], Julio Candela [1] and Luis Zamudio [2]

[1] Physical Oceanography Department, CICESE, Carretera Ensenada-Tijuana No. 3918, Zona Playitas, Ensenada, Baja California C.P. 22860, Mexico; mxcali@cicese.mx (V.M.G.); mgross@cicese.edu.mx (M.S.G.); malope@cicese.mx (M.L.-M.); anahi.berom@gmail.com (A.B.-R.); jcandela@cicese.mx (J.C.)

[2] Center for Ocean-Atmospheric Prediction Studies, Florida State University, Tallahassee, FL 32306-2840, USA; Luis.Zamudio.ctr@nrlssc.navy.mil

* Correspondence: vmagar@cicese.edu.mx; Tel.: +52-1646-175-0500

† These authors contributed equally to this work.

Received: 13 February 2020; Accepted: 25 February 2020; Published: 2 March 2020

Abstract: We analyzed the peak spring tidal current speeds, annual mean tidal power densities (TPD) and annual energy production (AEP) obtained from experiment 06.1, referred as the "HYCOM model" throughout, of the three dimensional (3D), global model HYCOM in an area covering the Baja California Pacific and the Gulf of California. The HYCOM model is forced with astronomical tides and surface winds alone, and therefore is particularly suitable to assess the tidal current and wind-driven current contribution to in-stream energy resources. We find two areas within the Gulf of California, one in the Great Island Region and one in the Upper Gulf of California, where peak spring tidal flows reach speeds of 1.1 m per second. Second to fifth-generation tidal stream devices would be suitable for deployment in these two areas, which are very similar in terms of tidal in-stream energy resources. However, they are also very different in terms of sediment type and range in water depth, posing different challenges for in-stream technologies. The highest mean TPD value when excluding TPDs equal or less than 50 W m^{-2} (corresponding to the minimum velocity threshold for energy production) is of 172.8 W m^{-2}, and is found near the town of San Felipe, at (lat lon) = (31.006–114.64); here energy would be produced during 39.00% of the time. Finally, wind-driven currents contribute very little to the mean TPD and the total AEP. Therefore, the device, the grid, and any energy storage plans need to take into account the periodic tidal current fluctuations, for optimal exploitation of the resources.

Keywords: tidal power density; in-stream renewable energy; peak spring tide flow; annual energy production; gulf of California

1. Introduction

Tides, winds, and density gradients contribute to the generation, the characteristics, and the evolution of ocean currents, but their percentage contribution may vary in space and time. In the open ocean, tidal currents are assumed to play a small role because the water depth is usually large. In contrast, in estuaries, inlets, and marginal seas, the tidal amplitudes and speeds increase due to funnelling and resonance effects caused by the bathymetry and the geometry of the basin. Tidal currents can be identified very easily in in-situ measurements or numerical simulations, because the tidal forcing is harmonic with well defined frequencies given by the tidal potential [1,2]. However, in general it is more complex to separate the residual current into wind-driven and density-driven components, except when one develops or applies a numerical model that is only forced with tides

and with surface wind fields. Two of such models have been found in the literature, one is the global HYCOM model reported in [3,4], and the other is the regional Delft3D model reported in [5]. In this work we will use the global HYCOM model, because with a global model other authors can replicate more easily our analysis at other sites around the world.

From a renewable energy characterization perspective, there are multiple studies that have assessed water level ranges for tidal barrages or tidal lagoons [6–8], and tidal and marine current speeds for in-stream device deployments [9–12], at different sites. Tidal barrages and lagoons exploit potential energy, while in-stream devices exploit hydrokinetic energy. Most studies focus on either tidal lagoons or in-stream devices only, because generally the best energy exploitation sites for each of these types of marine renewable energy (MRE) do not overlap. Also, the energy conversion devices themselves, together with the necessary infrastructure, may be different. Here we focus on hydrokinetic energy generation, and specifically on tidal and wind-driven current energy resources.

From an economic perspective it makes more sense to consider one development at a time, and ensure best return on investment before moving on. However, in some specific cases, such as in the MERMAID project (see http://www.vliz.be/projects/mermaidproject/), assessing a combination of options for the development of Multi-Use Platforms at Sea (MUPS) is the main deliverable, and some case studies within MERMAID have considered co-location of wind and wave conversion devices [13], for example. Some companies are exploring whether combining these technologies is financially robust (see http://www.floatingpowerplant.com/), but most studies conclude that such combinations are financially sound for co-location of multiple users, such as marine renewable energy, aquaculture and platform related transport, rather than co-location of different renewable energy technologies [14,15].

The purpose of this paper is to characterize the tidal currents and wind-driven currents in the Gulf of California, with some comments about tidal resources in the Baja Californian Pacific, and analyze their respective contributions to in-stream renewable energy generation. This is relevant to the MRE Industry because it informs them on most appropriate development sites in the region, and they can adapt their technological developments based on the findings. It is also relevant from a scientific point of view, because there are very few studies focusing on this particular issue, either under climatologically normal or under extreme conditions. The paper is organized as follows. In Section 2, we present the model validations, and evaluate the contribution of the barotropic tidal currents and the wind-driven currents to the mean peak flow speeds, in-stream power density, and annual energy production. In Section 3, we describe the HYCOM model configuration used in this work. We also describe the in-situ measurements and the methodology adopted for the verification of the model predictions. In Section 4, we close with some concluding remarks.

2. Results and Discussion

The HYCOM model is used to analyse the percentage contributions to Tidal Power Density (TPD) and Annual Energy Production (AEP), of the wind-driven currents and the tidally-driven currents. The analysis is performed over the domain and with the bathymetry shown in Figure 1. The red markers in the Great Island Region (GIR) correspond to ADCP moorings in the San Lorenzo Channel (SLC), the San Esteban Channel (SEC), the Ballenas Channel (BC). and the Delfin Sill (DS). Another ADCP mooring near Isla San Jorge (ISJ) was also used for verification.

2.1. Verification of Model Predictions against In-Situ Measurements

Figure 2 shows the vertically-integrated flow speed obtained with the HYCOM model (in red) and the measurements (in dashed blue) from the 1st of October to the 16th of October 2011, in the San Esteban Channel (SEC) mooring (shown in Figure 1). The verification is carried out for the barotropic tidal currents only, and to compare the hourly tidal current time series obtained from the measurements to those from the model, the former had to be reconstructed for the period of simulation of the latter, i.e., for the period between 01/10/2011 01:00:00 and 01/10/2012 00:00:00—this is explained in more detail in Section 3. Table 1 shows the yearly average of the modelled (mod) and measured (obs)

values (shown next to each other in "mod/obs" format) of $\overline{U}$ (see Equation (1)), $\overline{TPD}$ (see Equation (2)), the AEP (see Equation (3)), the relative error RE_x (see Equation (5)) and the $RMSE_x$ (see Equation (6)) for $x = \overline{U}$ and $x = \overline{TPD}$, as well as the correlation coefficient $\rho_{X,Y}$ (see Equation (4)), at the five verification sites. In the GIR $\rho_{X,Y}$ is either 0.91 or 0.92, and it is 0.71 at ISJ. $\rho_{X,Y}$ is much lower at ISJ because the bathymetry used by the model in the region of San Jorge Bay is not as good as the bathymetry used in the GIR. Please note that no results of the RE or $RMSE$ for AEP are shown because they are the same as for the TPD.

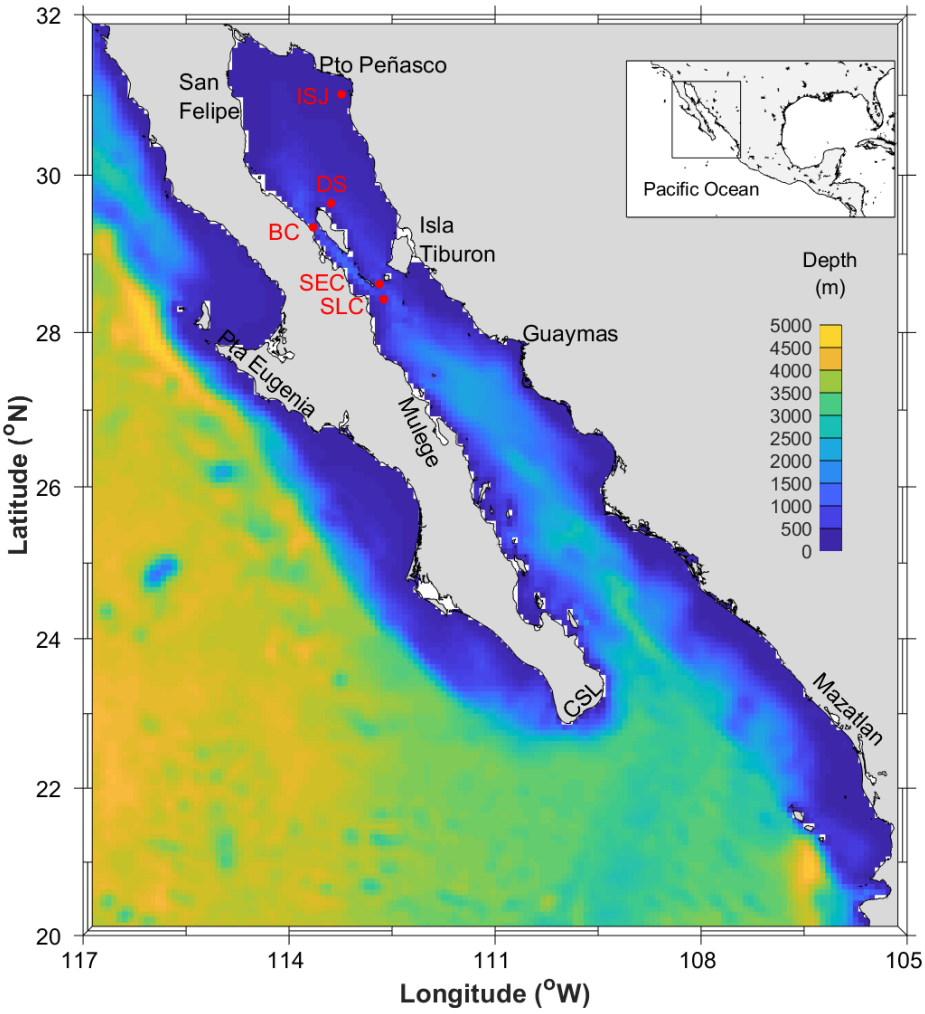

Figure 1. Model domain and bathymetry with markers showing ADCP moorings.

Table 1. Verification table for mean values.

Units: U $[\mathrm{m\,s^{-1}}]$, TPD $[\mathrm{W\,m^{-2}}]$, AEP $[\mathrm{kWh\,m^{-2}}]$, RE [%], RMSE_U $[\mathrm{m\,s^{-1}}]$, RMSE_{TPD} $[\mathrm{W\,m^{-2}}]$								
Mooring	$\overline{U}$ **mod/obs**	$\overline{TPD}$ **mod/obs**	**AEP mod/obs**	$\rho_{X,Y}$	RE_U	RE_{TPD}	RMSE_U	RMSE_{TPD}
ISJ	0.202/0.206	7.56/10.48	66.45/92.07	0.71	2.0%	27.8%	9.1×10^{-2}	14.13
DS	0.182/0.182	7.44/7.67	65.35/67.33	0.92	0.2%	3%	4.8×10^{-2}	6.05
BC	0.190/0.360	8.69/60.60	76.33/532.3	0.92	47%	86%	21×10^{-2}	98.2
SEC	0.372/0.417	56.28/85.24	494.4/748.7	0.91	10.8%	34%	11.7×10^{-2}	63.98
SLC	0.263/0.388	21.98/72.75	193.1/639.1	0.92	32.2%	69.8%	17.3×10^{-2}	102.0

The model underestimates $\overline{U}$ and $\overline{TPD}$ at all verification sites. The agreement is significantly worse at BC and at SLC, the two moorings furthest to the west. However, good agreement between model and observations is obtained at DS, ISJ and SEC. We also have significantly worse agreement at

BC and at SLC for the annual mean maximum spring tide speeds and TPD, shown in Table 2, but the RE_U and $RMSE_U$ at the other three sites, are less than 10% and less than 3.7×10^{-1} m s^{-1}, respectively.

Table 2. Verification table for mean maximum spring tidal values.

Units: U $[\mathrm{m\,s^{-1}}]$, TPD $[\mathrm{W\,m^{-2}}]$, RMSE_U $[\mathrm{m\,s^{-1}}]$, RMSE_{TPD} $[\mathrm{W\,m^{-2}}]$						
Mooring	$\overline{U}_{STM}$ **mod/obs**	$\overline{TPD}_{STM}$ **mod/obs**	RE_U	RE_{TPD}	RMSE_U	RMSE_{TPD}
ISJ	0.415/0.459	38.76/55.80	9.8%	30.6 %	11.9×10^{-2}	38.56
DS	0.417/0.399	39.6/35.62	−4.6%	−11.2%	4.5×10^{-2}	12.23
BC	0.467/0.822	54.6/311.1	43.2%	82.5%	36.7×10^{-2}	290.2
SEC	0.866/0.928	347.4/437.7	6.6%	20.6%	8.3×10^{-2}	119.36
SLC	0.568/0.918	101.7/436.7	38.2%	76.7%	36.8×10^{-2}	390.6

The $RMSE_U$ in Table 2 are of the same order as those reported in Defne et al. [11] for their tidal resource characterization study along the coast of Georgia (USA), and although we considered a different study site and we used a different model, this shows that the model predictions are reliable.

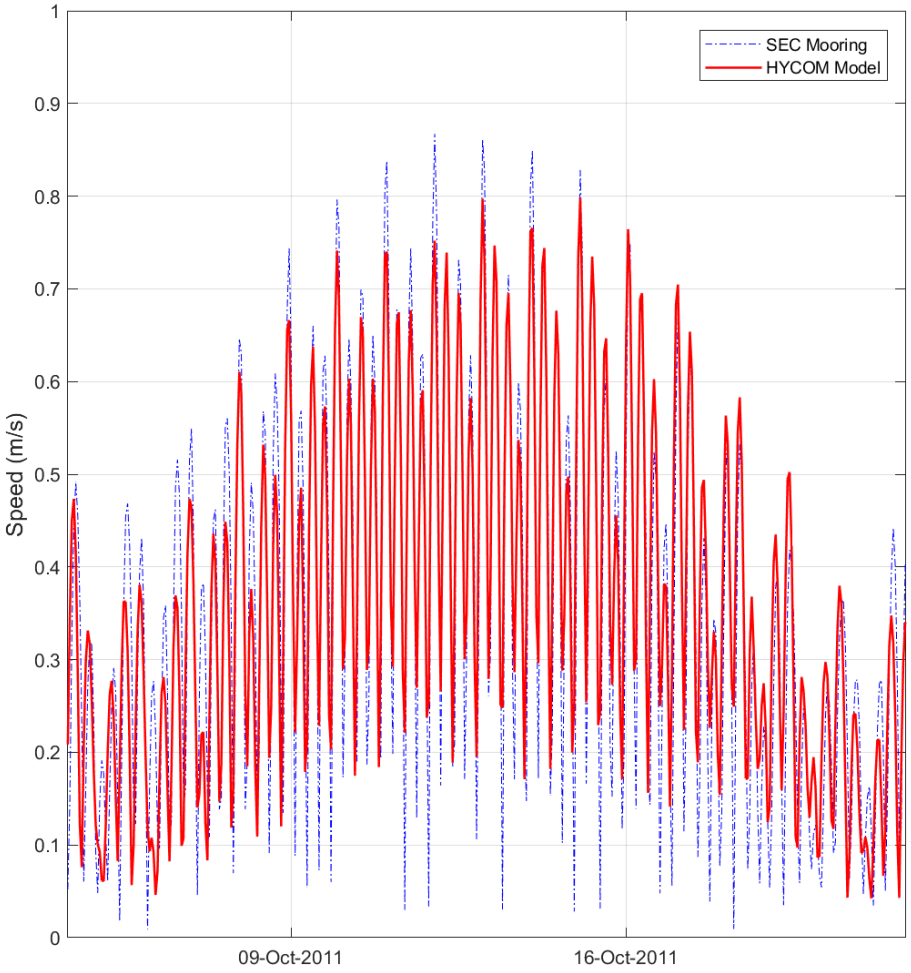

Figure 2. Tidal harmonic reconstruction of the modelled (solid red) and measured (dashed blue) tidal speed $[\mathrm{m\,s^{-1}}]$ time series at the SEC mooring, for the same two-week period.

2.2. Analysis of the Barotropic Tidal Signal

The map of $\overline{U}_{STM}$, the annual mean of the spring tide maxima, is shown in Figure 3. The map shows two regions with $\overline{U}_{STM}$ values close to 1 m s^{-1}. These two regions define two approximate transects that are shown in Figure 4.

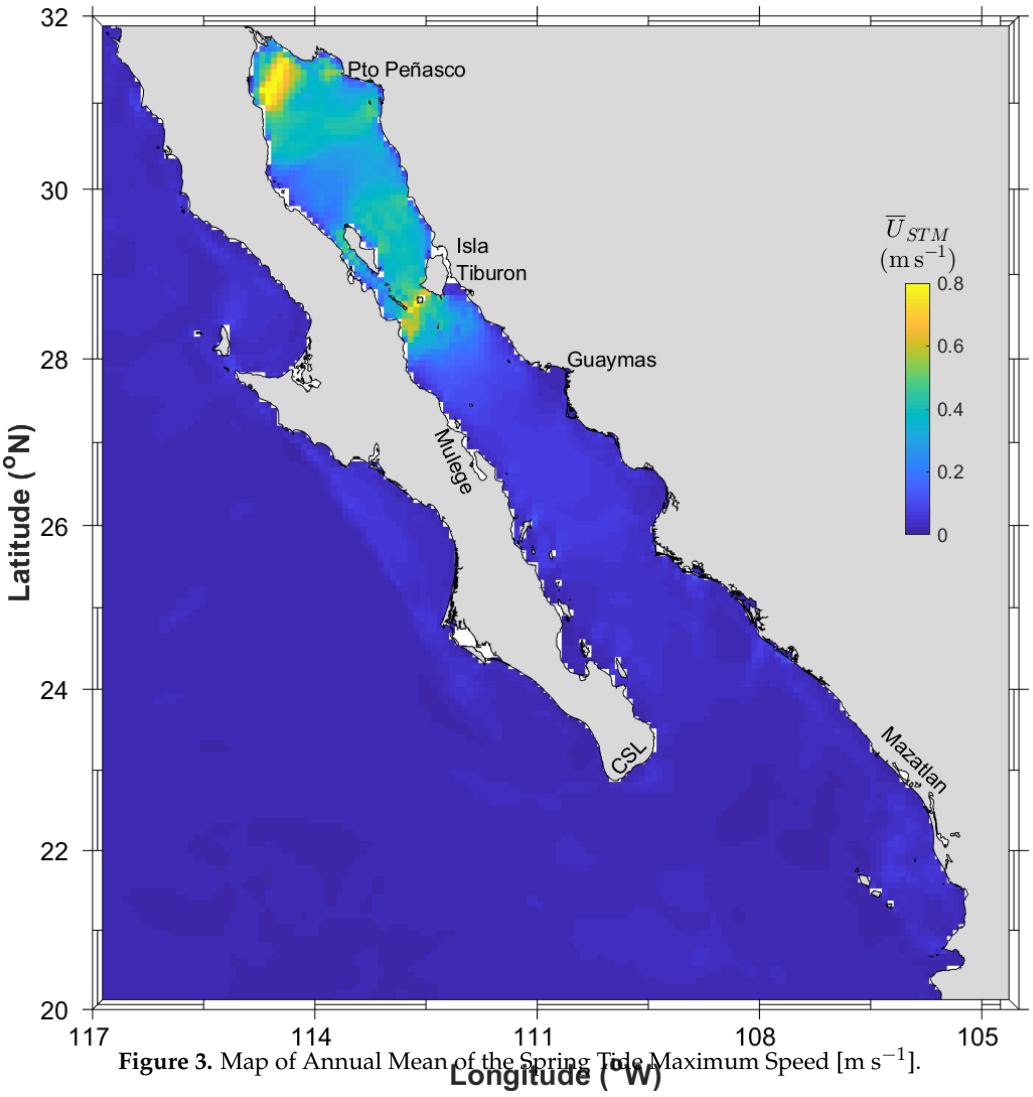

Figure 3. Map of Annual Mean of the Spring Tide Maximum Speed [m s^{-1}].

The first region is in the Upper Gulf of California, in the Colorado River Delta approach in the North, approximately along a transect running between San Felipe (SF) and El Tornillal, shown on the left of Figure 4. The second region is in the GIR, approximately along a transect joining Punta San Francisquito (PSF) to the western shore of Tiburón Island (TI), shown on the right of Figure 4. These landmarks are also shown in the first close-up figure, corresponding to Figure 5. Now, although most tidal stream devices operate at mean spring tidal speeds of 2.5 m s^{-1} or larger, some devices can operate at locations where spring tidal currents are as low as 1.3 m s^{-1} [16,17], and where depths are between 60 m and 120 m. It is possible that such values of $\overline{U}_{STM}$ are reached in the Upper Gulf or in the Great Island Region. The location where the model predicts a maximum of U_{max} is near San Felipe, and this maximum is of 1.11 m s^{-1} (see Table 3), which is not far from the minimum threshold of the GreenDeep device [17]. There are three other location where U_{max} is above one. However, the model used here predicts $\overline{U}_{STM}$ values between 0.8 m s^{-1} and 0.9 m s^{-1}. Tidal energy developers need to design technologies that can exploit lower flow speeds than first generation devices. Higher resolution

models need also to be developed in order to characterize the flow speeds with better spatial detail, in particular in the GIR.

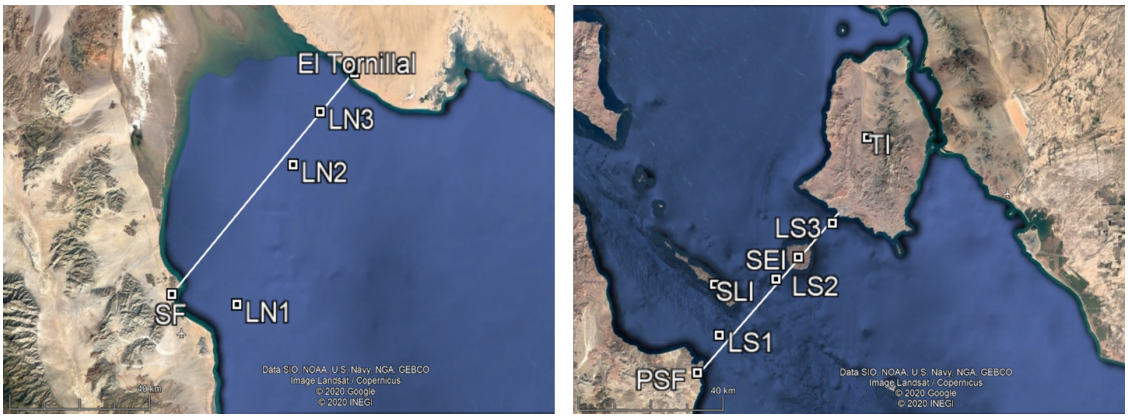

Figure 4. Northern (**left**) and southern (**right**) regions with largest tidal current speeds, with geographical markers for: San Felipe (SF), El Tornillal, Punta San Francisquito (PSF), San Lorenzo Island (SLI), San Esteban Island (SEI), and Tiburón Island (TI). The six locations with highest tidal current speeds are also shown.

Figure 5 shows the regions where TPD reaches values above 50 W m^{-2}, and the resulting annual mean of those values, defined as $\overline{TPD_{>50}}$. We chose 50 W m^{-2} because it corresponds to a minimum threshold speed, U_m of 0.46 m s^{-1}, which is roughly the minimum speed at which Tidal Energy Converters (TECs) start reacting to the flow and produce energy. Any speeds below U_m do not contribute to $\overline{TPD}$ or the AEP. This minimum threshold defines the regions with no commercially viable mean tidal power density. Based on the HYCOM model, such non-commercially viable regions appear as blank patches in Figure 5. The model defines a transect that joins (lat lon) = (28° N 112° 45′ 54.5″ W) in the Peninsula to (lat lon) = (28° 27′ 05.7″ N 111° 41′ 07.8″ W) on mainland Sonora, in the Gulf of California. According to the model, any commercially viable regions for tidal energy exploitation in the Gulf of California would be located north of this transect. According to the model as well, except for the Colorado River Delta Approach, there are very few places with water depths below 50 m which are commercially viable. However, as discussed by Magar [18], there are some known exploitable locations in the Channel between Tiburón Island and mainland Sonora. Therefore, the HYCOM model may serve as a guidance to identify some locations with exploitable resources, but has some limitations at shallow water depths, which may only be solved with better bathymetric data, and models with higher resolution. It may be noted that the only location in the Baja Californian Pacific that may have exploitable tidal energy resources, would be the channel just north of Punta Eugenia (shown in Figure 5), as the small colored area in the Baja Californian Pacific coast suggests. However, the sites along this coast will not be discussed further in this paper.

Figure 6 shows the percentage time (%T) when $TPD > 50$ W m^{-2}. The best locations in terms of percentage time would correspond to those with largest %T. Along the San Francisquito—Tiburón Island transect (the southern transect), the three most relevant locations are LS1, LS2 and LS3 (ordered from west to east), their details are in Table 3. Along the San Felipe—El Tornillal transect (the northern transect), the three most relevant locations are LN1, LN2 and LN3 (ordered from west to east), their details are summarized in Table 3. These six locations are highlighted as void circles in Figure 6.

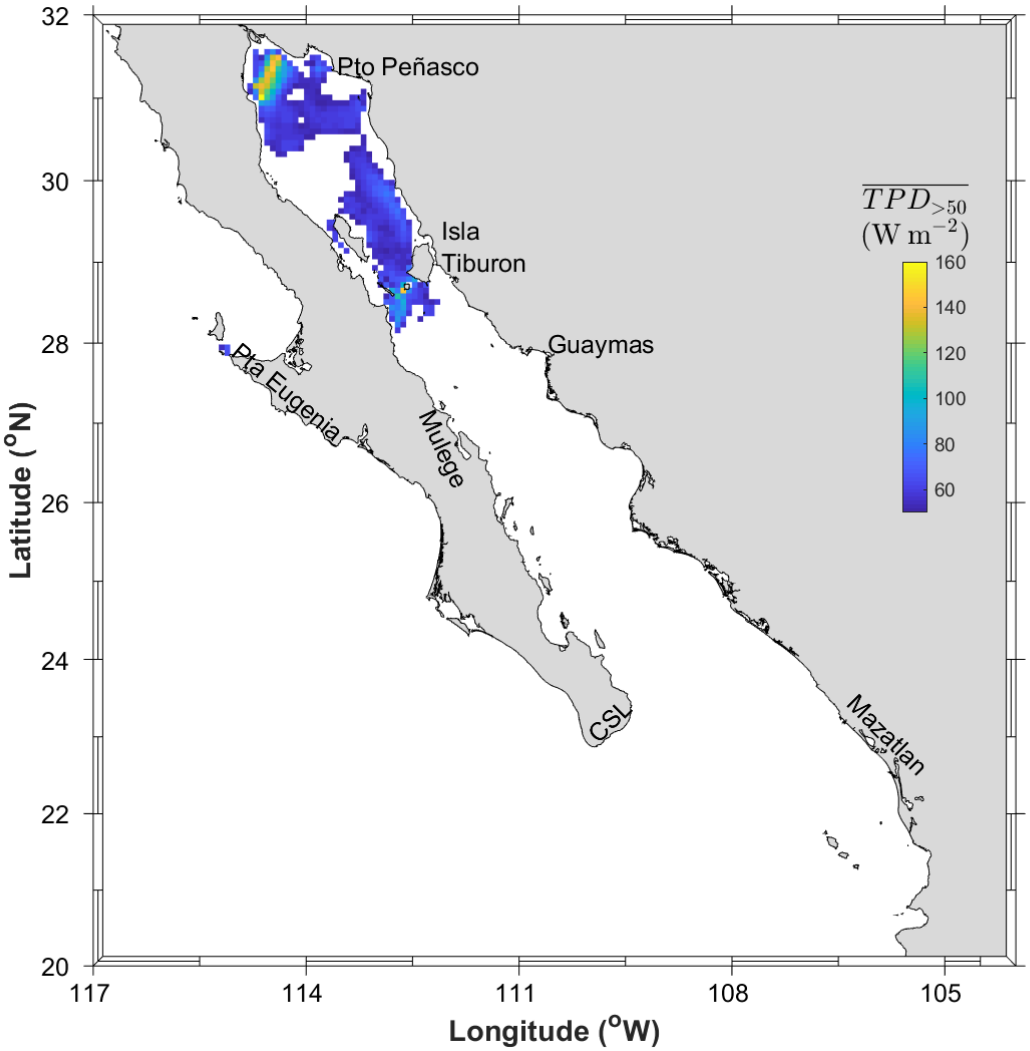

Figure 5. Map of $\overline{TPD_{>50}}$, corresponding to the mean of TPD when $TPD > 50$ W m^{-2}.

Table 3. Locations with largest six maximal speeds, U_{max}, over the simulation year.

Units: U $[\mathrm{m\,s^{-1}}]$ and TPD $[\mathrm{W\,m^{-2}}]$					
Location	**(lat lon)**	$\overline{U}_{STM}$	$\%T$	$\overline{TPD_{>50}}$	U_{max}
LN1	(31.006–114.64)	0.899	39.00	172.8	1.11
LN2	(31.348–114.48)	0.800	33.58	145.1	1.02
LN3	(31.480–114.40)	0.758	31.1	141.62	1.02
LS1	(28.506–112.80)	0.733	23.54	106.7	0.89
LS2	(28.646–112.64)	0.858	33.34	145.1	1.04
LS3	(28.786–112.48)	0.676	17.30	92.94	0.83

In terms of barotropic mean tidal power density, the two transects that we have identified are very similar, with slightly lower $\overline{TPD_{>50}}$ values in the southern transect compared to the northern one. However, the tidal range, the water depth, and the characteristics of the seafloor are distinctly different. The southern transect changes drastically from very shallow to depths of several hundred meters, has a seafloor composed of sand and rocks [19], and the tidal range is mostly below 2 m (check the tidal charts produced by CICESE for the tidal gauges in the GIR, by consulting: http://predmar.cicese.mx/). In contrast, the northern transect is macrotidal and with water depths mostly below 50 m, with seafloor

composed of cohesive and sandy sediments, and a tidal range that can reach around 6 to 7 m [20,21]. The difference in water depths and seabed sediment composition has important implications on the type of TEC that can be installed. In particular, the TEC moorings would need to be designed differently, and a detailed bathymetry would need to be generated in order to find the locations with depths that are appropriate for deployment. This is not in any way a limitation of the sites, but an opportunity for device and device deployment innovation [22], from 2nd (Gen2) to 5th (Gen5) Generation tidal turbine systems [23], and for local scale site characterization studies [24].

Figure 6 shows the percentage time, $\%T$, when the barotropic TPD is above 50 W m^{-2}, within the Gulf of California and for latitudes above the 28° parallel. The two transects that have been discussed previously stand out significantly in Figure 6, in particular the locations along these transects with $\overline{TPD_{>50}}$ above 140 W m^{-2}. The most energetic cells are LN1 near San Felipe in the northern transect, where $\overline{TPD_{>50}} = 172.8$ W m^{-2}, and LS2 and LN2, where $\overline{TPD_{>50}} = 145.1$ W m^{-2}. LS2 is between San Esteban Island (SEI) and San Lorenzo Island (SLI)—shown on the left of Figure 4, and LN2 is approximately midway between San Felipe and El Tornillal, in the Upper Gulf—shown on the right of Figure 4. At these three locations, the $\%T$ when $TPD > 50$ W m^{-2} is above to 30%.

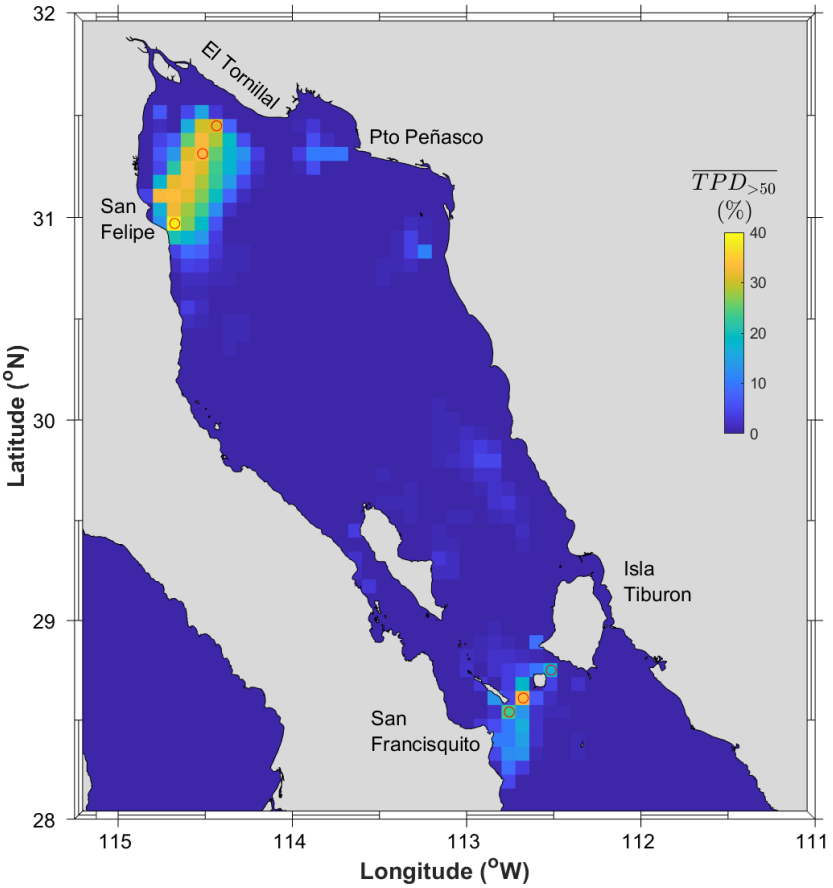

Figure 6. Map of percentage time $\%T$ when $TPD > 50$ W m^{-2}. The red circles correspond to the six most energetic locations, defined in the text.

Figure 7 shows the tidal AEP when considering only values of TPD above 50 W m^{-2}. In the regions where production is largest (in the region closest to San Felipe), we reach AEP values of 592 kWh m^{-2} yr^{-1}. One tidal stream device with a cross-section diameter of 20 m, or a cross-sectional area of $A = 314.16$ m^2,and an efficiency C_p of 0.35 [25,26], would produce a technical AEP of around 65 MWh yr^{-1}. A Mexican household requires an average of 1.7 to 3.9 MWh yr^{-1} [27], depending on their consumption habits, so one device may supply enough energy for 16 to 38 households. In order to

produce a minimum of 1.0 TWh yr^{-1}, a minimum of 15 devices with a 20 m diameter and an efficiency of at least 35% would be required, conservatively providing enough energy for 240 to 570 households. As the coastal regions are mostly rural, and with poor transmission line development [28], the energy produced should be consumed locally, to reduce costs. A tidal farm with 15 devices would be large enough for that purpose, but it would need to be combined with other energy sources and with energy storage systems.

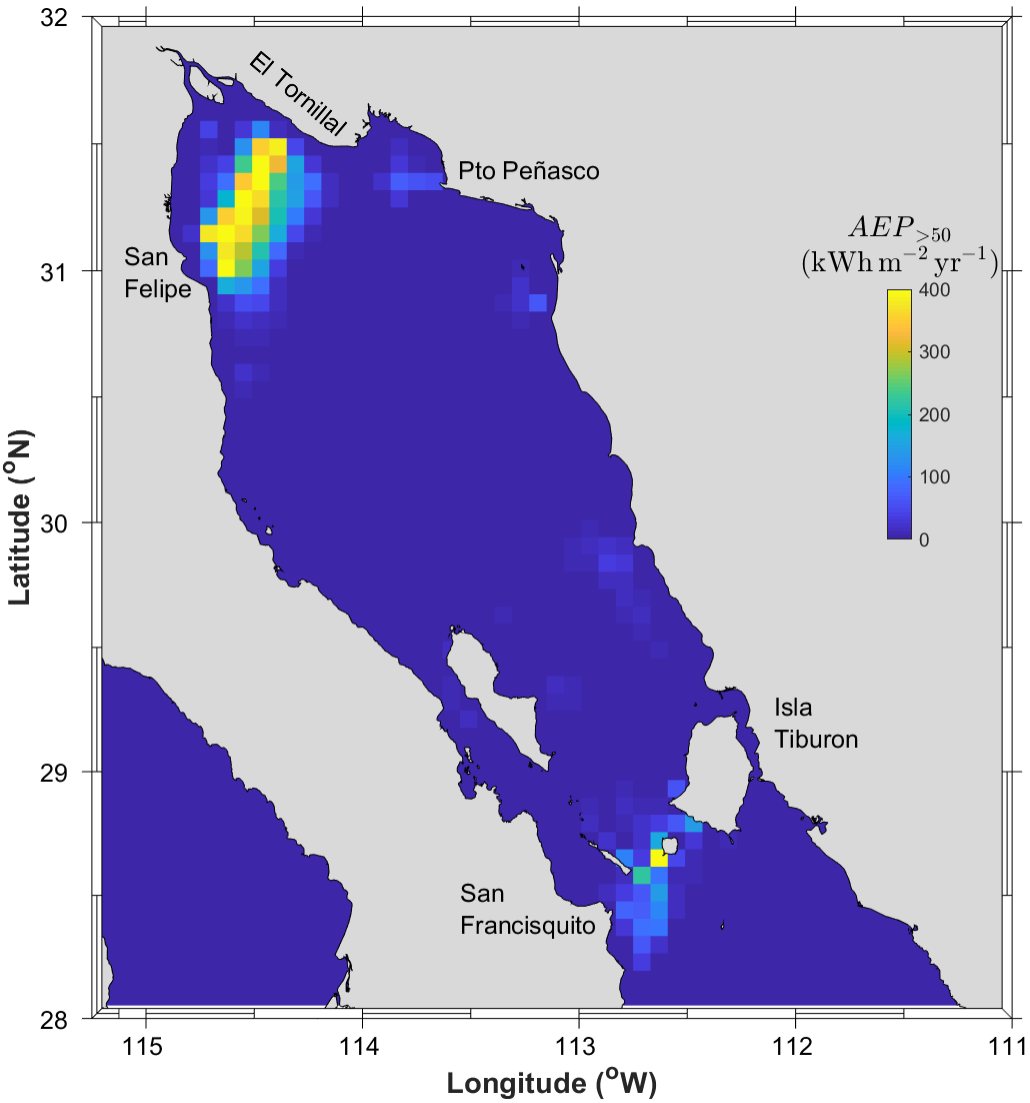

Figure 7. Map of AEP when $TPD > 50$ W m^{-2}.

2.3. Analysis of the Wind-Driven In-Stream Energy Resource Contribution

The plots in Figure 8 show the residual $\overline{TPD}$ at 0 m, 60 m, 100 m, and 200 m below Mean Sea Level. This residual $\overline{TPD}$ is linked to the wind-driven currents generated by the Navy Global Environmental Model (NAVGEM) forcing. The plots show a region between Mulegé and Guaymas, another region near the southern tip of the Baja California Peninsula, and some locations along the southern transect, joining San Francisquito to Tiburón Island (identified in the barotropic tides analysis), where $\overline{TPD} \approx$ 20 W m^{-2}. From the plots in Figure 8, we deduce that the $\overline{TPD}$ due to the wind forcing is either around or less than 20 W m^{-2}. This is much lower than the economically viable threshold of 50 W m^{-2} assumed earlier. Therefore, these $\overline{TPD}$ values are on their own too low for energy generation, but in locations

where tidal currents are strong, such as in the Punta San Francisquito to Tiburón Island transect, they may play some role in enhancing the tidal energy densities and the annual energy production.

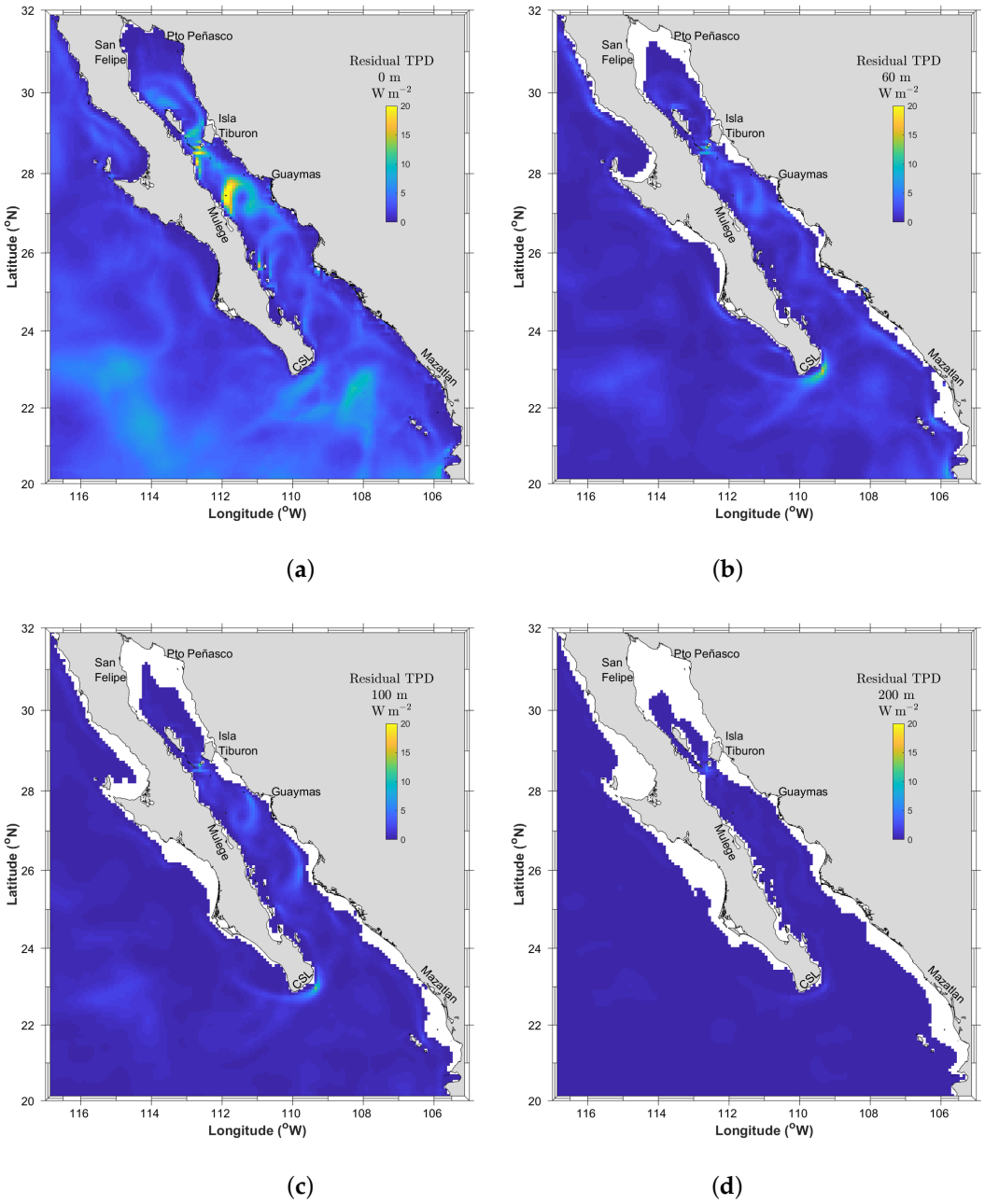

Figure 8. Residual $\overline{TPD}$ at (**a**) 0 m, (**b**) 60 m, (**c**) 100 m, and (**d**) 200 m below Mean Sea Level.

Finally, the plots in Figure 9 show the relative importance of the AEP produced by the wind-driven currents in relation to the total AEP. The areas where the contribution of the wind-driven current to the total AEP is really small are also areas with large in-stream tidal energy resources, and where discussed in Section 2.2. The AEP is dominated by the wind-driven component almost everywhere south of the 28° parallel, except for the region in the Baja Californian Pacific that was briefly mentioned at the end of Section 2.2. As the annual $\overline{TPD}$ is less than 20 W m^{-2}, it is not large enough to produce energy by itself. Therefore, the results indicate that the locations for best in-stream energy resource exploitation are still the two transects identified in Section 2.2.

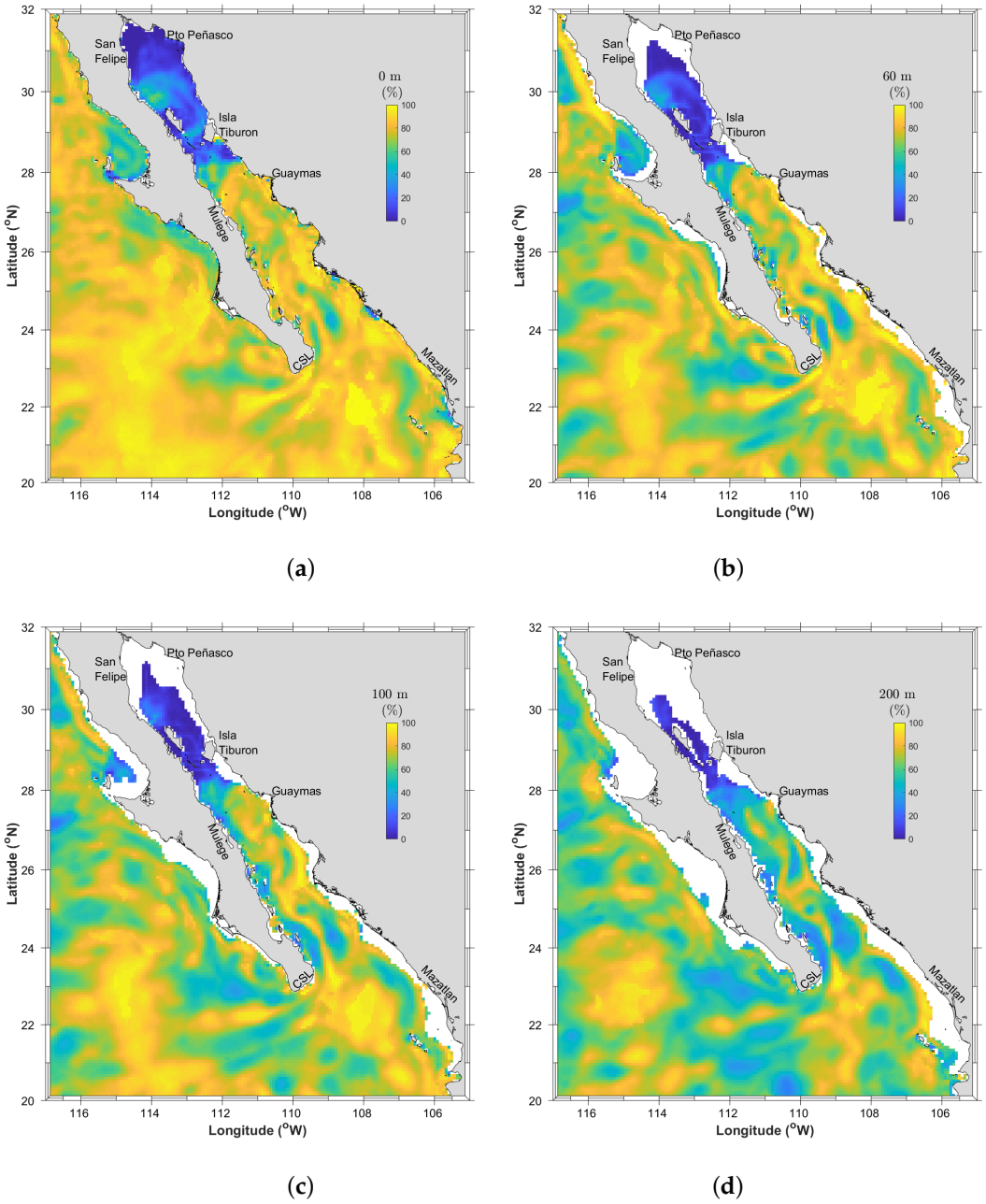

Figure 9. Relative importance of residual *AEP* against total *AEP* at (**a**) 0 m, (**b**) 60 m, (**c**) 100 m, and (**d**) 200 m below Mean Sea Level.

3. Materials and Methods

The "Hybrid Coordinate Ocean Model", referred to as HYCOM since its inception [29], was developed as an outgrowth of the "Miami Isopycnic Coordinate Ocean Model", or MICOM, described in Bleck et al. [30]. The model is a primitive equation model with two prognostic equations for the horizontal velocity components (which we express in terms of the velocity vector), one representing the mass continuity or layer-thickness tendency, one for salinity and one for temperature.

The HYCOM experiment we used employs atmospheric forcing from the Navy Global Environmental Model (NAVGEM) [31], and geopotential tidal forcing from the five largest principal tidal components: M_2, S_2, N_2, K_1 and O_1. A self-attraction and load (SAL) term is added to the tidal forcing. The SAL term accounts for the self-gravitation of the tidally deformed ocean and solid

earth [32], and for the load deformations of the solid earth [33]. The model has a nominal horizontal resolution of $1/12.5^\circ$ at the equator and 41 isopycnal layers in the vertical. The NAVGEM has a horizontal resolution of 0.33°, and is interpolated to the finer resolution of the hydrodynamic grid for the simulations. First, the model is run from 1996 to 2003 with a climatological forcing, then from 2003 to 2011 with the atmospheric forcing from the Navy Operational Global Atmospheric Prediction System, NOGAPS [34], and finally, the atmospheric NAVGEM forcing is applied after 30 June 2011. Tidal forcing is initiated on 3 July 2011. Global three-dimensional fields are stored every hour for one year, from 1 October 2011 to 1 October 2012. More details can be found in [3,4].

The analysis is performed over the domain and with the bathymetry shown in Figure 1, which is the ETOPO1 bathymetry with some sounding corrections in the Great Island Region (GIR) courtesy of CICESE (Zamudio, *pers. comm.*), described in [35]. The GIR moorings were deployed during the "umbrales" (2002–2006) project; these moorings were first reported in [36,37]. The ISJ mooring was deployed between June 2017 and November 2017 during the "CeMIE-Océano" (2017–2021) project, and was first reported in [38].

The in-situ data mentioned above were used to verify the model predictions in the GIR and in ISJ. Since the modelling period extended between 01/10/2011 01:00:00 and 01/10/2012 00:00:00 in hourly timesteps, but the ADCP data were collected at different periods, the verification analysis of the model against the data was performed for the period modelled in the simulations, and focused on the depth-averaged tidal signal alone. The tidal principal component analyses for the ADCP and the simulation results were performed with the T_TIDE tidal analysis package [2], and the tidal signal was reconstructed from the tidal principal components for the simulation period. From this reconstruction, we computed the annual mean tidal speed $\overline{U}$, the annual mean tidal power density $\overline{TPD}$, and the annual energy power AEP:

$$\overline{U} = \frac{1}{N}\sum_{i=1}^{N} U_i, \tag{1}$$

$$\overline{TPD} = \frac{1}{2N}\rho\sum_{i=1}^{N} U_i^3, \text{ and} \tag{2}$$

$$AEP = \frac{1}{2}\rho\sum_{i=1}^{N} U_i^3, \tag{3}$$

with $U_i = \sqrt{u_i^2 + v_i^2}$, $N = 8784$ (2012 is a leap year), and $\rho = 1024\,\mathrm{kg\,m^{-3}}$ is the water density. $\overline{U}$, $\overline{TPD}$, and AEP are computed for the model (mod) and the mooring (obs) data, at each mooring location.

The agreement between model $X = x_{mod}$ and observation $Y = x_{obs}$ was assessed using the Pearson correlation coefficient, $\rho_{X,Y}$, defined as [39]:

$$\rho_{X,Y} = \frac{\mathrm{cov}(X,Y)}{\sigma_X \sigma_Y}, \tag{4}$$

where cov is the covariance between the two time series, and σ_X and σ_Y the standard deviations of X and Y, respectively; the relative error RE_x,

$$RE_x = \left\| \frac{\overline{x}_{obs} - \overline{x}_{mod}}{\overline{x}_{obs}} \right\|; \tag{5}$$

and the root mean square error $RMSE_x$,

$$RMSE_x = \sqrt{\frac{1}{N}\sum_{i=1}^{N} (x_{i,obs} - x_{i,mod})^2}, \tag{6}$$

over the simulation period. Once the model was validated at the mooring locations, we analysed the field maps of $\overline{U}$, $\overline{TPD}$, and AEP, as well as the annual means of the spring tide maxima, $\overline{U}_{STM}$ and $\overline{TPD}_{STM}$, to determine the best sites for tidal and wind-driven current energy extraction, based on $\overline{U}$, $\overline{TPD}$, and AEP. We also assessed the percentage contribution of each of them throughout the case study domain, and discuss some implications for tidal and wind-driven current power generation. It is worth noting that here we will not consider any techo-economic or socio-ecological constraints, but the analysis would be similar to that for wind energy resource characterization studies developed in previous work [28,40].

4. Conclusions

Data from a global HYCOM model with tide and wind forcings and no data assimilation was used to make a mesoscale evaluation of in-stream renewable energy resources in the Gulf of California and the Baja Californian Pacific. Specifically, the model was used to separate and analyze the tidal and wind-driven current speeds, tidal power densities, and annual energy production in the region. The model showed there are two areas within the Gulf of California, one in the Great Island Region and one in the Upper Gulf of California, with mean annual tidal power densities between 141 and 173 W m^{-2}. At some locations in these areas, energy would be produced for around 31% to 39% of the year, with technologies that can generate electricity above a minimum speed threshold of 0.46 m s^{-1}, equivalent to a minimum TDP threshold of 50 W m^{-2}. The in-stream energy resources are strongly dominated by the tidal stream component, with wind-driven current speeds associated with TPDs generally below 20 W m^{-2}, which is below the minimum TPD threshold for energy generation. The installation of 15 devices with a diameter of 20 m and an efficiency of 35% would provide enough energy for 240 to 570 households. These devices could be installed along two transects, either between San Felipe and El Tornillal in the Upper Gulf of California, or between San Francisquito and Tiburón Island, in the Great Island Region. Subsequent studies may either assess the suitability for marine renewable energy developments from a socio-economic perspective, or improve the speeds, TPD and AEP assessments by using a model with higher spatial resolution at the two relevant transects identified in this paper.

Author Contributions: Conceptualization, V.M. and M.S.G.; methodology, V.M. and L.Z.; software, L.Z.; validation, M.L.-M. and V.M.G.; formal analysis, V.M.; data curation, A.B.-R., M.L.-M. and V.M.G.; resources, J.C.; writing–original draft preparation, V.M.; writing–review and editing, all authors; visualization, V.M.G and V.M.; project administration, V.M.; funding acquisition, V.M. All authors have read and agreed to the published version of the manuscript.

Funding: This work was partially supported by the SENER-CONACYT grant no. 249795, within the project "CeMIE-Océano" (2017-2021).

Acknowledgments: Thanks to the Department of Physical Oceanography of CICESE, and in particular technician Erick Rivera-Lemus, for his support with fieldwork and data acquisition. Thanks to the waves group of CICESE (led by Paco Ocampo), for support with technician time and batteries provided for instrumentation. Thanks to the Oceanographic Equipment Coordination and the CANEK group of CICESE, for support with equipment and equipment maintenance resources. HYCOM simulation was performed on the Navy Department of Defense (DoD) Supercomputing Resources at Stennis Space Center, Mississippi, using grants of computer time from the DoD High Performance Computing Modernization Program. Thanks to the anonymous reviewers for their comments.

Conflicts of Interest: The authors declare no conflict of interest. The funders had no role in the design of the study; in the collection, analyses, or interpretation of data; in the writing of the manuscript, or in the decision to publish the results.

Abbreviations

The following abbreviations are used in this manuscript:

ADCP	Acoustic Doppler Current Profiler
AEP	Annual Energy Production
BC	Ballenas Channel
DS	Delfin Sill

ETOPO1	Earth topography and bathymetry global relief model, at 1 arc-minute resolution
GIR	Great Island Region
HYCOM	Hybrid Coordinate Ocean Model
ISJ	Isla San Jorge
LN	Location North
LS	Location South
MICOM	Miami Isopycnic Coordinate Ocean Model
MRE	Marine Renewable Energy
MUPS	Multi-Use Platforms at Sea
NAVGEM	Navy Global Environmental Model
NOGAPS	Navy Operational Global Atmospheric Prediction System
PSF	Punta San Francisquito
SAL	self-attraction and load
SEC	San Esteban Channel
SF	San Felipe
SLC	San Lorenzo Channel
TI	Tiburón Island
TPD	Tidal Power Density
T_TIDE	Tidal Harmonic Analysis Toolbox

References

1. Parker, B.B. (Ed.) *Tidal Hydrodynamics*; Wiley: Hoboken, NJ, USA, 1991.
2. Pawlowicz, R.; Beardsley, B.; Lentz, S. Classical tidal harmonic analysis including error estimates in MATLAB using T_TIDE. *Comput. Geosci.* **2002**, *28*, 929–937. [CrossRef]
3. Buijsman, M.C.; Arbic, B.K.; Richman, J.G.; Shriver, J.F.; Wallcraft, A.J.; Zamudio, L. Semidiurnal internal tide incoherence in the equatorial Pacific. *J. Geophys. Res. Ocean.* **2017**, *122*, 5286–5305. [CrossRef]
4. Arbic, B.K.; Alford, M.H.; Ansong, J.K.; Buijsman, M.C.; Ciotti, R.B.; Farrar, J.T.; Hallberg, R.W.; Henze, C.E.; Hill, C.N.; Luecke, C.A.; et al. A Primer on Global Internal Tide and Internal Gravity Wave Continuum Modeling in HYCOM and MITgcm. In *New Frontiers in Operational Oceanography*; GODAE OceanView; Florida Climate Institute: Gainesville, FL, USA, 2018. [CrossRef]
5. Gross, M.; Magar, V. Wind-Induced Currents in the Gulf of California from Extreme Events and Their Impact on Tidal Energy Devices. *J. Mar. Sci. Eng.* **2020**, *8*, 80. [CrossRef]
6. Dupont, F.; Hannah, C.G.; Greenberg, D. Modelling the sea level of the upper Bay of Fundy. *Atmosphere-Ocean* **2005**, *43*, 33–47. [CrossRef]
7. Hiriart Le Bert, G. Potencial energético del Alto Golfo de California. *Boll. Soc. Geológ. Mex.* **2009**, *61*, 143–146. [CrossRef]
8. Xia, J.; Falconer, R.A.; Lin, B. Hydrodynamic impact of a tidal barrage in the Severn Estuary, UK. *Renew. Energy* **2010**, *35*, 1455–1468. [CrossRef]
9. Carbajal, N.; Backhaus, J.O. Simulation of tides, residual flow and energy budget in the Gulf of California. *Oceanol. Acta* **1998**, *21*, 429–446. [CrossRef]
10. Garrett, C.; Cummins, P. The power potential of tidal currents in channels. *Proc. R. Soc. A Math. Phys. Eng. Sci.* **2005**, *461*, 2563–2572. [CrossRef]
11. Defne, Z.; Haas, K.A.; Fritz, H.M. Numerical modeling of tidal currents and the effects of power extraction on estuarine hydrodynamics along the Georgia coast, USA. *Renew. Energy* **2011**, *36*, 3461–3471. [CrossRef]
12. Yang, X.; Haas, K.A.; Fritz, H.M. Theoretical Assessment of Ocean Current Energy Potential for the Gulf Stream System. *Mar. Technol. Soc. J.* **2013**, *47*, 101–112. [CrossRef]
13. Perez-Collazo, C.; Pemberton, R.; Greaves, D.; Iglesias, G. Monopile-mounted wave energy converter for a hybrid wind-wave system. *Energy Convers. Manag.* **2019**, *199*, 111971. [CrossRef]
14. Stuiver, M.; Soma, K.; Koundouri, P.; van den Burg, S.; Gerritsen, A.; Harkamp, T.; Dalsgaard, N.; Zagonari, F.; Guanche, R.; Schouten, J.J.; et al. The Governance of Multi-Use Platforms at Sea for Energy Production and Aquaculture: Challenges for Policy Makers in European Seas. *Sustainability* **2016**, *8*, 333. [CrossRef]

15. Dalton, G.; Bardócz, T.; Blanch, M.; Campbell, D.; Johnson, K.; Lawrence, G.; Lilas, T.; Friis-Madsen, E.; Neumann, F.; Nikitas, N.; et al. Feasibility of investment in Blue Growth multiple-use of space and multi-use platform projects; results of a novel assessment approach and case studies. *Renew. Sustain. Energy Rev.* **2019**, *107*, 338–359. [CrossRef]
16. Tweed, K. 2013. Underwater Kite Harvests Energy from Slow Currents—Could Kites be the Secret to Capturing Tidal Energy? Available online: https://spectrum.ieee.org/energywise/green-tech/geothermal-and-tidal/underwater-kite-harvests-energy-from-slow-currents (accessed on 19 November 2019).
17. Minesto. 2019. The Future of Renewable Energy. Available online: https://www.minesto.com/our-technology (accessed on 19 November 2019).
18. Magar, V. Tidal Current Technologies. In *Sustainable Energy Technologies*; CRC Press: New York, NY, USA, 2017; pp. 293–308. [CrossRef]
19. Byrne, J.V.; Emery, K.O. Sediments of the Gulf of California. *Geol. Soc. Am. Bull.* **1960**, *71*, 983.[983:sotgoc]2.0.co;2. [CrossRef]
20. Morales Pérez, R.A.; Gutiérrez de Velazco Sanromán, G. Mareas en el Golfo de California. *Geofísica Int.* **1989**, *28*, 25–46.
21. Álvarez, L.G.; Suárez-Vidal, F.; Mendoza-Borunda, R.; González-Escobar, M. Bathymetry and active geological structures in the Upper Gulf of California. *Boll. Soc. Geológ. Mex.* **2009**, *61*, 129–141. [CrossRef]
22. Corsatea, T.D.; Magagna, D. *Overview of European Innovation Activities in Marine Energy Technology*; Technical report; Environmental Sciences Group: Brussels, Belgium, 2014.
23. Verdant Power. 2019. Technology Advancement. Available online: https://www.verdantpower.com/technology-adv (accessed on 21 November 2019).
24. LeGrand, C. *Assessment of Tidal Energy Resource—Marine Renewable Energy Guides*; Technical Report; Black and Veatch Ltd.: London, UK, 2009.
25. Myers, L.; Bahaj, A. Power output performance characteristics of a horizontal axis marine current turbine. *Renew. Energy* **2006**, *31*, 197–208. [CrossRef]
26. Iyer, A.; Couch, S.; Harrison, G.; Wallace, A. Variability and phasing of tidal current energy around the United Kingdom. *Renew. Energy* **2013**, *51*, 343–357. [CrossRef]
27. Oropeza-Perez, I.; Petzold-Rodriguez, A. Analysis of the Energy Use in the Mexican Residential Sector by Using Two Approaches Regarding the Behavior of the Occupants. *Appl. Sci.* **2018**, *8*, 2136. [CrossRef]
28. Magar, V.; Gross, M.; González-García, L. Offshore wind energy resource assessment under techno-economic and social-ecological constraints. *Ocean Coast. Manag.* **2018**, *152*, 77–87. [CrossRef]
29. Bleck, R. An oceanic general circulation model framed in hybrid isopycnic-Cartesian coordinates. *Ocean Model.* **2002**, *4*, 55–88. [CrossRef]
30. Bleck, R.; Rooth, C.; Hu, D.; Smith, L.T. Salinity-driven Thermocline Transients in a Wind- and Thermohaline-forced Isopycnic Coordinate Model of the North Atlantic. *J. Phys. Oceanogr.* **1992**, *22*, 1486–1505.<1486:sdttia>2.0.co;2. [CrossRef]
31. Hogan, T.F.; Liu, M.; Ridout, J.A.; Peng, M.S.; Whitcomb, T.R.; Ruston, B.C.; Reynolds, C.A.; Eckermann, S.D.; Moskaitis, J.R.; Baker, N.L.; et al. The Navy Global Environmental Model. *Oceanography* **2014**, *27*, 116–125. [CrossRef]
32. Ray, R.D. Ocean self-attraction and loading in numerical tidal models. *Mar. Geod.* **1998**, *21*, 181–192. [CrossRef]
33. Hendershott, M.C. The Effects of Solid Earth Deformation on Global Ocean Tides. *Geophys. J. Int.* **1972**, *29*, 389–402. [CrossRef]
34. Rosmond, T.; Teixeira, J.; Peng, M.; Hogan, T.; Pauley, R. Navy Operational Global Atmospheric Prediction System (NOGAPS): Forcing for Ocean Models. *Oceanography* **2002**, *15*, 99–108. [CrossRef]
35. Argote, M.L.; Amador, A.; Lavín, M.F.; Hunter, J.R. Tidal dissipation and stratification in the Gulf of California. *J. Geophys. Res.* **1995**, *100*, 16103. [CrossRef]
36. López, M.; Candela, J.; Argote, M.L. Why does the Ballenas Channel have the coldest SST in the Gulf of California? *Geophys. Res. Lett.* **2006**, *33*. [CrossRef]
37. López, M.; Candela, J.; García, J. Two overflows in the Northern Gulf of California. *J. Geophys. Res.* **2008**, *113*. [CrossRef]

38. Bermúdez-Romero, A.; Magar, V.; Gross, M.S.; Godínez, V.M.; López-Mariscal, M.; Rivera-Lemus, E. Characterization of in-stream tidal energy resources in the Gulf of California: Implementation, calibration and validation of a hydrodynamic model. In Proceedings of the 13th European Wave and Tidal Energy Conference (EWTEC2019), European Wave and Tidal Energy Conference Series, Napoli, Italy, 1–6 September 2019.
39. Pearson, K. Mathematical Contributions to the Theory of Evolution. III. Regression, Heredity, and Panmixia. *Philos. Trans. R. Soc. A Math. Phys. Eng. Sci.* **1896**, *187*, 253–318. [CrossRef]
40. Magar, V.; González-García, L.; Gross, M.S. Evaluación Técnico-económica del Potencial de Desarrollo de Parques Eólicos en Mar: El Caso del Golfo de California. *BIOtecnia* **2017**, *19*, 3–8. [CrossRef]